Pure Appl. Geophys.

https://doi.org/10.1007/s00024-024-03619-5

Pure and Applied Geophysics

Modified Parameterization Scheme of Orographic Gravity Waves in the SOCOL Chemistry-Climate Model

A. V. Koval,[1] N. M. Gavrilov,[1] V. A. Zubov,[1,2] E. V. Rozanov,[1,3] and A. G. Golovko[1]

Abstract—This paper describes the results of modifying the parametrization of subgrid stationary orographic gravity waves (OGWs) in the chemistry-climate model SOCOL, version 3. The originally used OGW parameterization is modified using polarization relations for stationary waves in the rotating atmosphere. Parameterizing the OGW generation by the Earth's topography at subgrid scales follows the widely used Lott and Miller scheme, but the expressions for calculating the vertical profiles of OGW amplitudes, wave drag and heat influx, are modified. Test simulations of the general atmospheric circulation for 10 years (from 2009 to 2018) have been launched with the SOCOL model involving the modified OGW parameterization. Using the realistic profiles of the background wind and temperature, characteristics of OGWs propagating in the atmosphere from the Earth's surface to the heights of about 80 km are simulated for different locations in the Northern and Southern Hemispheres. Comparisons with the MERRA2 reanalysis data show that the modified OGW parameterization provides better agreement of simulated and observed multiyear-mean zonal wind and temperature in the mesosphere and lower thermosphere region. The modified parameterization can be used in other atmospheric circulation models.

Keywords: Orographic gravity waves, mesoscale atmospheric waves, subgrid scale orography, mountain wave drag, wave heating rates, atmospheric circulation.

1. Introduction

Internal gravity waves (IGWs) play an important role in the formation of the general circulation, temperature regime, and the composition of the middle and upper atmosphere. One of the important and permanent IGW sources is the Earth's topography. As a result of the interaction of atmospheric flows with inhomogeneities of the Earth's relief, mesoscale stationary orographic gravity waves (OGWs) are generated. Recently, a number of projects have been dedicated to studying the effects of OGWs in various atmospheric layers, for example, the Deep Propagating Gravity Wave Experiment—DEEPWAVE (Fritts et al., 2018). The wave acceleration (drag) of the mean horizontal wind maximizes during winter seasons, when the eastward-directed mean winds at all altitudes from the surface to the lower thermosphere allow the vertical propagation of stationary OGWs (e.g., Gavrilov et al., 2015; Hoffmann et al., 2013).

Under certain conditions, OGWs can propagate into the mesosphere, and even to the lower thermosphere (e.g., Fritts et al., 2018; Kaifler et al., 2015). For instance, based on the results of studies within the DEEPWAVE program in New Zealand, Fritts et al. (2018) noted that if the stratospheric wind is strong enough, OGWs grow rapidly with height and break due to their large amplitudes in the stratosphere. When the wind is weak, waves can penetrate higher into the mesosphere. However, the dynamic and energetic impact of OGWs in the mesosphere and thermosphere has not yet been studied properly so far.

The OGW drag influence the zonal wind and may contribute to changes in the atmospheric refractive index for planetary waves (Alexander et al. 2010). An important feature of OGWs is their strong impact on the Brewer–Dobson circulation in the stratosphere (Butchart, 2014). Also, mesospheric OGW and PW drag is responsible for formation of the effect of elevated stratopause after the sudden stratospheric

[1] Saint-Petersburg University, Saint Petersburg, Russia. E-mail: a.v.koval@spbu.ru; n.gavrilov@spbu.ru; v_zubov@rambler.ru; Eugene.Rozanov@pmodwrc.ch

[2] Voeikov Main Geophysical Observatory, Saint Petersburg, Russia.

[3] Physikalisch-Meteorologisches Observatorium Davos/World Radiation Center (PMOD/WRC), Davos, Switzerland.

Published online: 12 December 2024

warming events (Limpasuvan et al., 2012). Using various methods, OGW manifestations were observed in the troposphere (e.g., Beer, 1974; Scorer, 1949), in the stratosphere (Eckermann & Preusse, 1999; Fritts et al., 2018; Jiang et al., 2002; Preusse et al., 2002) and in the mesosphere (e.g., Heale et al., 2020).

Orographic waves and their possible impacts on the thermal regime and dynamics of the lower thermosphere have been studied in the regions over the Ural Mountains (Semenov et al., 1981; Shefov & Pertsev, 1984), over the Caucasus Range (Sukhodoev & Yarov, 1998), over Antarctica (Alexander & Teitelbaum, 2007) and over the mountain ranges of South America (Smith et al., 2009). These experimental data indicated the existence of quasi-stationary temperature disturbances with amplitudes of about 10 °K above mountain systems at altitudes of 80–90 km. Shefov et al. (1999) estimated the spatial distribution of OGW energy fluxes with the average magnitudes $\sim$ 3 mW/m^2 in the mesopause region above the leeward side of a mountain range.

Many modern models of global atmospheric circulation, do not have sufficient spatial resolution for direct reproduction of mesoscale OGWs. Various parameterization schemes were developed and used to describe accelerations and heat influxes produced by upward propagating subgrid OGWs in the atmosphere (e.g., Kim & Arakawa, 1995; Lott & Miller, 1997; Gregory et al., 1998; Scinocca & McFarlane, 2000; Webster et al., 2003; Kim et al., 2003; Kim & Doyle, 2005; Choi & Hong, 2015; Xu et al., 2017; Van Niekerk et al. 2020). These schemes take into account various details of the processes of propagation and impact of OGWs in the atmosphere. In particular, one of the widely used schemes is the Lott and Miller (1997) parameterization of the subgrid-scale orography, in which OGWs produce a drag on the mean flow when a critical level is reached or when waves become unstable and break. The paper by Kuchar et al. (2020) presents a study of OGW impacts on atmospheric circulation, and also presents a detailed comparison of the data simulated with the Canadian Middle Atmosphere Model and the MERRA-2 reanalysis data.

In recent years, there has been an understanding that a parameterization of orographic drag in general circulation models could be a significant source of uncertainty, and the parameterized OGW effects can differ in different models (Butchart et al., 2011; Van Niekerk et al., 2018). In order to minimize inconsistencies in the reproduction of OGW effects in various models, an ambitious project "COnstraining ORographic Drag Effects" (COORDE) was launched for comparing various parameterizations of orographic drag, as well as for comparing the results of parameterization of OGW effects with simulations using high-resolution models having the horizontal grid spacing of the order of 1 km (van Niekerk et al., 2018, 2020).

Gavrilov and Koval (2013) developed a modification of widely used OGW parameterization by Lott and Miller (1997). The modification gives more detailed vertical structure of wave drag and heat influxes based on polarization relations for stationary OGWs taking account the Earth rotation (e.g., Gossard & Hooke, 1975). This modified parameterization was used for simulating the general circulation of the middle atmosphere with the Middle and Upper Atmosphere Model – MUAM (Gavrilov et al., 2015). In particular, it was shown that under certain conditions the impact of OGWs can lead to changes in the amplitudes of planetary waves (PWs) exceeding 50% (Gavrilov et al., 2015).

This study is dedicated to the implementation of the modifications in OGW parameterization made by Gavrilov and Koval (2013) to the chemistry-climate model SOCOL, version 3 (SOCOL3). In Sect. 2, we briefly describe main modifications in the Subgrid Scale Orographic Parameterization (SSOP), which is currently used in the SOCOL3 model to calculate the dynamic and thermal effects of OGWs propagating in the atmosphere from the Earth's surface to the heights of the lower thermosphere. In Sect. 3 we consider vertical structure of OGW parameters in different regions obtained with the modified parameterization using realistic fields of wind and temperature simulated with the SOCOL3 model. Section 4 is devoted to the influence of modifications in the OGW parameterization on the mean fields of zonal wind and temperature in the middle atmosphere simulated with the SOCOL3 model.

2. *Modifications of the Parameterization of Orographic Gravity Wave Effects*

Stationary mesoscale perturbations arising due to interactions between the mean flow and the Earth's topography can be attributed to stationary IGWs with observable frequencies $\sigma = 0$. Usually, horizontal wavenumbers $k^2 > f^2/c_s^2$ and vertical wavenumbers $m^2 > > 1/(2H)^2$, where H is the pressure scale height, c_s is the speed of sound, f is the Coriolis parameter.

2.1. *Vertical Structure of OGW Dynamical and Thermal Effects*

When IGW propagates in the inhomogeneous atmosphere with dissipation, momentum and energy exchanges occur between the mean flow and waves leading to wave accelerations of the mean flow and heating/cooling of the atmosphere. Gavrilov and Koval (2013) developed a simple scheme describing vertical structure of dynamic and thermal effects of stationary OGW, which we use here for the modification of OGW parameterization used currently in the SOCOL3 model. Gavrilov and Koval (2013) used IGW polarization relations for the rotating plane atmosphere and obtained the following expressions for stationary waves with $\sigma = 0$, $|m| > > 1/(2H)$ and $k^2 > > f^2/c_s^2$:

$$m^2 = \frac{N^2}{\overline{v}_\xi^2}\left(1 - \frac{f^2}{k^2\overline{v}_\xi^2}\right)^{-1}; \qquad a_{w\xi} = -\frac{m^2U^2}{(2\overline{v}_\xi)}, \ (v_z + \kappa_z)\left(1 + \frac{1}{(\gamma - 1)\mathrm{Pr}}\right) \tag{1}$$

where $\overline{v}_\xi$ and $a_{w\xi}$ are components of the mean wind and wave acceleration along the horizontal axes ξ directed along the horizontal wave vector; U is the amplitude of wave variations of horizontal velocity; v_z and κ_z are total molecular plus turbulent vertical kinematic viscosity and heat conductivity, respectively; Pr is the Prandtl number; γ is the ratio of heat capacities; N is the Brunt-Vaisala frequency.

An important energetic characteristic, which is included into most recent parameterizations of IGW effects, is the heating/cooling impacts due to dissipation of wave energy (e.g., Yigit and Medvedev, 2009). It is commonly assumed that the wave heat influx is determined by the divergence of vertical wave enthalpy flux $F_t = \overline{\rho} c_p \overline{w'T'}$ (where T is temperature and c_p is the heat capacity at constant pressure, primes denote wave perturbations), which is sometimes called as "the sensible wave heat flux" (e.g., Hickey et al., 2011). Theory of IGWs in the hydrostatic atmosphere (e.g., Medvedev & Klaassen, 2003), indicates that wave variations T' and w' are shifted by $\pi/2$ in phase, so that $F_t = 0$ for non-dissipating waves and $F_t < 0$ when the atmosphere is dissipative. Akmaev (2007) found for a non-hydrostatic model that.

$$F_t = F_e + F_\theta \tag{2}$$

where $F_e = \overline{p_{w'}}$ is the vertical wave energy flux, and F_θ (proportional to $-\overline{\theta_{w'}}$, where θ is the potential temperature) may be called as the wave flux of potential enthalpy. According to Gavrilov (1990), $F_\theta = \overline{\rho}\gamma_a \overline{\varepsilon w'}$, where ε' is the wave part of heat influx caused by dissipative mechanisms. For IGWs without dissipation $\varepsilon' = 0$ and $F_\theta = 0$. Taking account of IGW dissipation, a number of authors (Akmaev, 2007; Hickey et al., 2011; Medvedev & Yiğit, 2019) showed that always the wave flux of potential enthalpy is downwards ($F_\theta < 0$) and produces cooling in the stable middle and upper atmosphere. The sign and direction of F_t depends on the relative values of F_e and F_θ in Eq. (2). The wave enthalpy flux $F_t > 0$, when $F_e > -F_\theta$, so that OGW produces the net heating of the atmosphere (Akmaev, 2007; Hickey et al., 2011). When $F_e < -F_\theta$ in Eq. (2), one has $F_t < 0$ and OGW may produce the net cooling of the atmosphere. Gavrilov and Popov (2022) obtained the following expression for the total wave-induced heating rate:

$$\varepsilon_w = c a_{w\xi} + \frac{1}{\overline{\rho}}\frac{\partial}{\partial z}\left(\overline{\left(\sigma'_{z\xi} + \tau'_{z\xi}\right)v'_\xi} - \frac{(\gamma - 1)\overline{\rho}\,\overline{T}}{gB}\overline{\left(\varepsilon'_t + \varepsilon'_m + \varepsilon'_r\right)s'}\right) \tag{3}$$

where c is the horizontal phase speed of wave; g is gravity acceleration; $B = \gamma - 1 + g^{-1}\partial c_s^2/\partial z$ is a parameter of static stability of the atmosphere; ε_t', ε_m', ε_r' are the wave components of heating rates due to turbulent and molecular viscosity, and radiative heat exchange, respectively. For stationary IGWs with $c = 0$ the first term in the right-hand side of

Eq. (3), is equal to zero, but dissipative and diabatic terms can provide local heating/cooling of the atmosphere in accordance with Akmaev (2007). Applying the polarization relations for OGWs in rotating atmosphere to Eq. (3) similar to Gavrilov and Koval (2013), one can get the following expression for the local heating rate produced by stationary OGW:

$$\varepsilon_w = \frac{1}{\overline{\rho}}\left(\delta v_z Z + \frac{\gamma H}{2(\gamma-1)}\frac{d}{dz}(\kappa_z Z)\right); \delta = \frac{f^2}{k^2}\frac{\partial}{\partial z}\left(\frac{\partial \overline{v}_\xi^2}{\partial z}\right)^{-1} \quad (4)$$

where $Z = \overline{\rho} m^2 U^2$. Eqs. (1) and (4) show that wave accelerations and heat influxes are nonzero only for dissipative and diabatic OGWs in accordance with the known non-acceleration theorem (Andrews et al., 1987). According to Eq. (4) at $\delta > 0$, OGW may produce local heating of the atmosphere, $\varepsilon_w > 0$. However, when δ becomes negative, OGW produce local cooling of the atmosphere. According to Gavrilov and Koval (2013), the vertical structure of the wave amplitude U in Eq. (1) and Eq. (4) can be described by the equation obtained from consideration of balance of wave energy and having the following form:

$$\frac{\partial}{\partial z}\left(\frac{\overline{\rho} f^2 U^2}{|k|N}\sqrt{1-\frac{f^2}{k^2 \overline{v}_\xi^2}}\right) = -2\overline{\rho}(\nu + K_z)\delta m^2 U^2 \quad (5)$$

For given vertical profiles of $\overline{v}_\xi$ and $\overline{T}$ and the wave amplitude U_0 at the lower boundary, Eq. (5) can be solved with respect to U^2. A finite-difference recurrent expression connecting U^2_{i+1} and U^2_i at $(i+1)$-th and i-th vertical grid nodes was described by Gavrilov and Koval (2013).

The condition of OGW convective stability is $\partial \overline{T}/\partial z + \partial T'/\partial z + \gamma_a > 0$, where T′ is wave temperature variation and $\gamma_a = g/c_p$ is adiabatic temperature gradient. For stationary OGWs with zero horizontal phase speed this condition is equivalent to $U < |\overline{v}_\xi|$. In the modified OGW parameterization, we put $U = |\overline{v}_\xi|$ locally in the regions of wave instability. Equation (1) and Eq. (4) have singularities at $|\overline{v}_\xi| \to f/|k|$, $|\overline{v}_\xi| \to 0$ and $\partial|\overline{v}_\xi|/\partial z \to 0$. The first case corresponds to the critical level, where linear IGW theory predicts $m^2 \to \infty$ in Eq. (1) and the instability and strong dissipation of shortened OGWs is assumed. This situation occurs in the vicinity of the level, where the horizontal wind becomes perpendicular to the direction of the OGW propagation ξ so that $|\overline{v}_\xi| \to 0$. In the present parameterization we use common assumption that $U = 0$ above the critical level. At heights, where $\partial|\overline{v}_\xi|/\partial z \to 0$, the magnitude of parameter δ in Eq. (4) may sharply increase. Our analysis showed that the distribution of δ values for grid nodes located at each height are close to normal, and when the δ value is outside the interval of three standard deviations from the respective mean value, we take δ to be equal to the closest boundary of this interval.

After obtaining the vertical profile of U^2 from Eq. (5), one can use Eq. (1) and Eq. (4) to calculate the vertical profiles of the wave drag $a_{w\xi}$ and heating rate ε_w. The lower boundary value of U_0, required for solving Eq. (5), is estimated using the parameterization of subgrid orography described below.

2.2. *Parameterization of Subgrid Orography*

The used parameterization of subgrid orography is essentially the same as is exploited in the current SSOP parameterization involved into the chemistry-climate SOCOL3 model. To parameterize the Earth's orography, the widely used method is applied, which was proposed by Baines and Palmer (1990) and then used by Lott and Miller (1997). This approach is based on the concept of "subgrid" orography having horizontal scales of changes in the Earth's surface height, which are smaller than the horizontal grid spacing of the numerical model. In the vicinity of each grid node, according to Lott and Miller (1997), an elliptical approximation of the subgrid-scale relief is used.

Forces acting on this elliptical barrier from the side of an oncoming horizontal flow were investigated by Scinocca and McFarlane (2000). The mountain barrier acts on the atmosphere with equal and opposite directed force, which can be considered as the vertical flux of the horizontal momentum $\boldsymbol{F_m}$ created by generated OGW. The components of this flux per unit area are directed against the oncoming flow, F_{mv}, and perpendicular to it, F_{mn}, and can be described by the following expressions (Baines &

Palmer, 1990; Gavrilov & Koval, 2013; Lott & Miller, 1997):

$$F_{mv} = \rho_0 v_0 N_0 \mu s G\left(B\cos^2\chi + C sin^2\chi\right)$$
$$F_{mn} = \rho_0 v_0 N_0 \mu s G(B - C)\sin\chi\cos\chi \quad (6)$$

where subscript zero denotes values at the lower boundary, i.e., at the first model level above the mean Earth relief; v_0 is the average horizontal wind velocity at the lower boundary; μ is the standard deviation of the subgrid variations of Earth's relief height; χ is the angle between the mean wind direction and the minor axis of the elliptical barrier; s is the standard deviation of the relief slope; G is the mountain sharpness parameter. For elliptical mountain profile, Lott and Miller (1997) proposed $G = 1.23$. Coefficients B and C in Eq. (6) are described by the following formulas: $B = 1 - 0.18\zeta - 0.04\zeta^2$, $C = 0.48\zeta + 0.3\zeta^2$, where ζ is the parameter characterizing the anisotropy (or aspect ratio) of the subgrid-scale relief.

Using Eq. (6), Gavrilov and Koval (2013) have got the following formulae for the effective horizontal wavenumber of the orographic wave, k_e, and the magnitude of the wave momentum flux, F_{m0}, at the lower boundary z_0 of the model:

$$k = k_e = \frac{2s\sqrt{F_{mv}^2 + F_{mn}^2}}{\rho_0 v_0 N_0 \mu^2 \cos\theta} \quad (7)$$

$$F_{m0} = \rho_0 \overline{v'_\xi w'} = \rho_0 U_0^2 \frac{\sqrt{k^2\bar{v}_{\xi 0}^2 - f^2}}{2N_0} \quad (8)$$

Using Eq. (6) and Eq. (8), one can determine the effective amplitude of the OGW U_0 at the low level. The values of k and U_0 calculated using Eq. (7) and Eq. (8) are used as a boundary condition for calculating U^2 using Eq. (5) at all nodes of the vertical grid. The mean wind projection, $\bar{v}_\xi$, on the direction of wave propagation in Eq. (5) is found as the sum of the projections of the mean zonal and meridional winds onto the direction of the lower boundary wave momentum flux.

2.3. The Chemistry-Climate Model SOCOL

The described above Modified Subgrid Orographic Parameterization (MSOP) of OGW effects was implemented into the chemistry–climate model SOCOL version 3, which is intensively used for model studies of SOlar Climate Ozone Links (Stenke et al., 2013). This model consists of the ECHAM5 general circulation model (GCM) and a modified chemistry module of the model for investigating ozone trends (MEZON) described by Egorova et al. (2003) and Schraner et al. (2008). They are interactively coupled via the transfer of the 3-dimensional fields of temperature and wind from GCM to MEZON, and via the transfer of concentrations of radiatively active water vapor, ozone, methane, nitrous oxide, and chlorofluorocarbons back from MEZON to GCM. The SOCOL3 model has 40 layers in vertical direction covering pressure range from the Earth's surface up to 0.01 hPa. The model can be run very efficiently in parallel mode. Its performance was successfully evaluated in the framework of International CCM Intercomparison projects: CCMVal2 (SPARC, 2010) and CCMI-1 (Hegglin et al., 2015). Detailed description of the SOCOL3 model was made by Stenke et al. (2013).

The SOCOL3 model involves the SSOP scheme for OGW effects implemented previously into the ECHAM (Roeckner et al., 2003), which is based on the approximation of the Earth's surface topography at subgrid scales using the method proposed by Lott and Miller (1997). SSOP involves calculation of momentum transfer from the Earth to the atmosphere produced by orographic gravity waves and the drag exerted by the subgrid scale mountains, when the air flow interacts with mountains at low levels. According ideas of saturated IGWs, the SSOP assumes that above the orographic source the OGW wave stress is constant and wave drag is zero, except when the waves reach a critical level or when they break. At a critical level OGW disappear and wave stress is set to zero above that level. Above the breaking level, at which Richardson number becomes smaller than a critical value, the gravity wave breaks and stress remains constant and equal to the stress at the breaking level (Roeckner et al., 2003).

The main difference between our MSOP and SSOP is using Eq. (5) for simulating vertical profiles of OGW amplitude and applying Eq. (1) and Eq. (3) to calculate wave accelerations and heat influxes at

each grid node of the model. In the analysis of the subgrid orography the only difference of the modified parameterizations is higher latitude–longitude resolution (2' × 2') of the used in the MSOP database of the Earth's relief ETOPO2 (2015) compared to the (10' × 10') resolution used in the SSOP. For molecular viscosity and heat conductivity MSOP uses the Sutherland expression (Kikoin, 1976). Vertical profiles of background turbulent viscosity are set having maxima of 10 m^2s^{-1} near the Earth's surface and 100 km, and a minimum of 0.1 m^2s^{-1} in the stratosphere (see Gavrilov et al., 2020).

The previous version of our OGW parameterization (Gavrilov & Koval, 2013) was mainly developed for using in a general circulation model of the middle and upper atmosphere, and the lower boundary for solving Eq. (5) was set at altitude of 7 km. At the MSOP the lower level value of U_0 in Eq. (8) is determined at the first vertical level of the SOCOL3 model above the Earth's surface at each horizontal grid node. This improves calculating the OGW impacts in the upper troposphere/lower stratosphere.

3. OGW Parameters in Realistic Background Fields

In this section we consider OGW characteristics obtained with the modified parameterization described in Sect. 2. Realistic global distributions of the background wind, pressure, and temperature for OGW simulations are obtained with the SOCOL3 model and correspond to January 2000. The data output has a time step of 12 h and a spatial resolution of 64 grid nodes along the meridian and 128 nodes along the parallel. The vertical grid contains 40 nodes in the isobaric coordinate. Figures 1 and 2 presents, respectively, the latitude–longitude distributions of the amplitude of wave variations of the horizontal wind velocity, U, and zonal component of wave drag, a_{wx}, produced by OGWs at heights of 20 and 50 km, averaged over January. According to Eq. (5), the vertical profile of OGW amplitude depends on the profiles of the background wind, temperature, turbulent and molecular viscosity, and thermal conductivity. At low dissipation near the Earth's surface, OGW amplitudes increase quasi-exponentially with height, and the regions of maximum wave

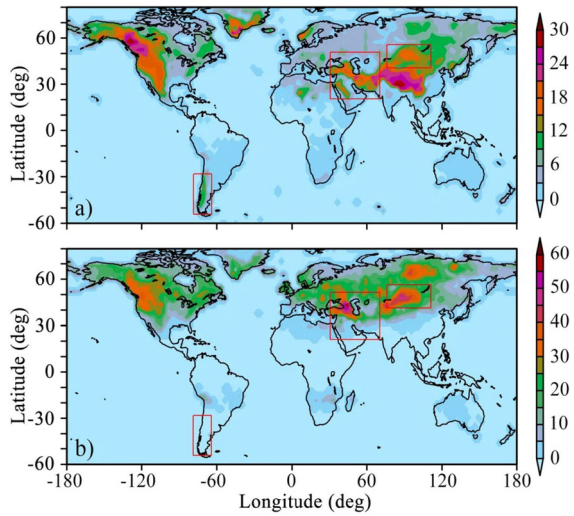

Figure 1
Latitude–longitude distributions of OGW horizontal velocity amplitude U ($m{\cdot}s^{-1}$) averaged for January at altitude 20 km (**a**) and 50 km (**b**). Rectangles denote geographic locations of the Middle East, Southern Siberia and Southern Andes—see clarification in the text

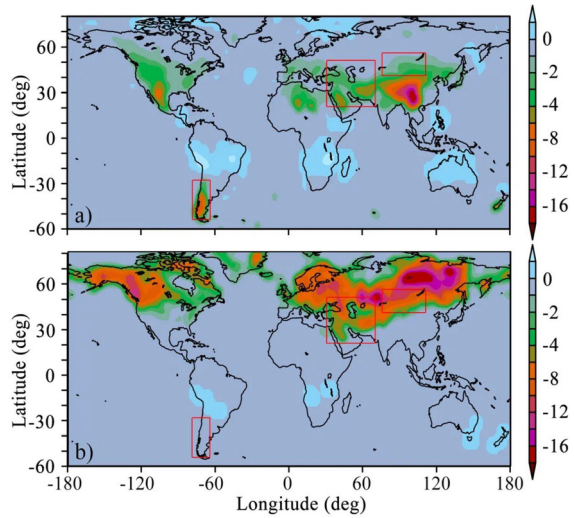

Figure 2
Same as Fig. 1 but for OGW zonal drag ($m{\cdot}s.^{-1}$/day)

amplitudes in Fig. 1a mainly correspond to areas of mountain systems.

OGW dissipation increases with height due to enhanced molecular and turbulent viscosity and heat conduction as well as due to increasing m^2 according to Eq. (1). In addition, some waves attenuate at the critical levels near the heights, where $|\overline{v}_\xi| \to 0$. A

reason for critical levels could be changes in wind direction with altitude. When the mean horizontal wind becomes perpendicular to the direction of wave propagation ξ, a critical level near the height of $\overline{v}_\xi = 0$ arises (see Sect. 2.1). Over large mountain systems, OGWs may have large amplitudes (such as over the Himalayas in Fig. 1a), which may increase as wave propagate upwards and produce convective instability and breaking, when waves become saturated in the unstable regions (see Sect. 2.1). This may explain the reduced maximum of OGW amplitude over the Himalayas at 50 rm altitude in Fig. 1b. Similar effects have already been discussed previously (e.g., Fritts et al., 2018, 2019; Heale et al., 2020).

Also, there is an additional reason for the change in OGW structures with height connected with the Earth's rotation. Equations (1), (4), (5) include the Coriolis parameter *f*, which is increased towards high latitudes and may contribute to the predominant propagation of OGWs in the middle atmosphere at high latitudes. Comparing Fig. 1a and 1b, one can see larger OGW amplitudes with maxima over Siberia and Greenland at altitude of 50 km relative to lower altitudes. As a result, Fig. 1b shows that areas of increased OGW amplitude at altitude of 50 km are not always located above the main mountain systems, which reflects the combined action of the mechanisms described above.

Figure 2 for the zonal component of OGW drag shows spatial distributions similar to the distributions of OGW amplitude in Fig. 1 for respective heights with larger OGW drag at higher northern latitudes. In Fig. 2b, the monthly mean values of OGW zonal drag can reach up to 20 $m{\cdot}s^{-1}$/day in the lower mesosphere corresponding to wave heat influxes up to several K/day. These values may be even higher at certain times and locations. Such substantial values confirm that orographic waves can significantly impact the dynamic and thermal regime of the middle atmosphere (e.g., Pertsev, 1989, 1997; Reichert et al., 2019). Wave accelerations of the order of 10 $m{\cdot}s^{-1}$/day in the stratosphere were obtained by Kuchar et al. (2020).

The distribution of OGW drag in the lower stratosphere shown in Fig. 2a also agrees well with that given by several OGW parameterizations and presented in Fig. 4 of the paper by Van Niekerk et al. (2020). Our estimate for amplitudes of OGW temperature variations are about 10–30 K, and the total vertical wave energy flux is about a few mW/m^2 at altitudes of 50–60 km above mountain systems, which corresponds in the order of magnitude to experimental estimates (e.g., Shefov et al., 1999; Sukhodoev & Yarov, 1998).

For a more detailed analysis of vertical profiles of OGW characteristics at different background conditions, we chose three different regions, which are marked by rectangles in Figs. 1, 2. The first one corresponds to the Middle East. We chose this latitude–longitude interval because the same one was used by Van Niekerk et al. (2020) in a comparative analysis of OGW drag given by various parameterizations. The second region corresponds to the Southern Siberia. We chose this region rather than the Himalayas and Tibet, because, as noted above, OGWs over the Himalayas may become unstable and break in the lower stratosphere without propagating to higher altitudes. To compare OGW propagation conditions in the Northern (winter) and Southern (summer) Hemispheres, a third region over the Southern Andes was selected.

Figure 3 represents vertical profiles of background horizontal wind components and temperature, as well as OGW parameters according to the modified OGW parameterization, averaged over the selected regions. Figure 3a shows the vertical profiles of the background zonal wind in the considered regions. It is clearly seen that in January, for winter conditions (Middle East and Southern Siberia), the wind direction is eastward at all altitudes, while in the summer Southern Hemisphere the zonal wind is directed to the west at altitudes above 20 km. At altitudes where the zonal wind tends to zero in the Southern Hemisphere, the critical levels occur, as discussed in Sect. 2.1. This corresponds to an increase in the vertical wavenumber shown in Fig. 3i and total decay of OGWs under the action of viscosity. Therefore, the total energy flux in Fig. 3h, components of OGW drag in Fig. 3d, e and heat influxes in Fig. 3f are equal to zero above 25 -30 km in the summer Southern Andes region.

The background meridional wind shown in Fig. 3b is subject to a strong longitudinal dependence associated with the impact of Rossby waves, so all

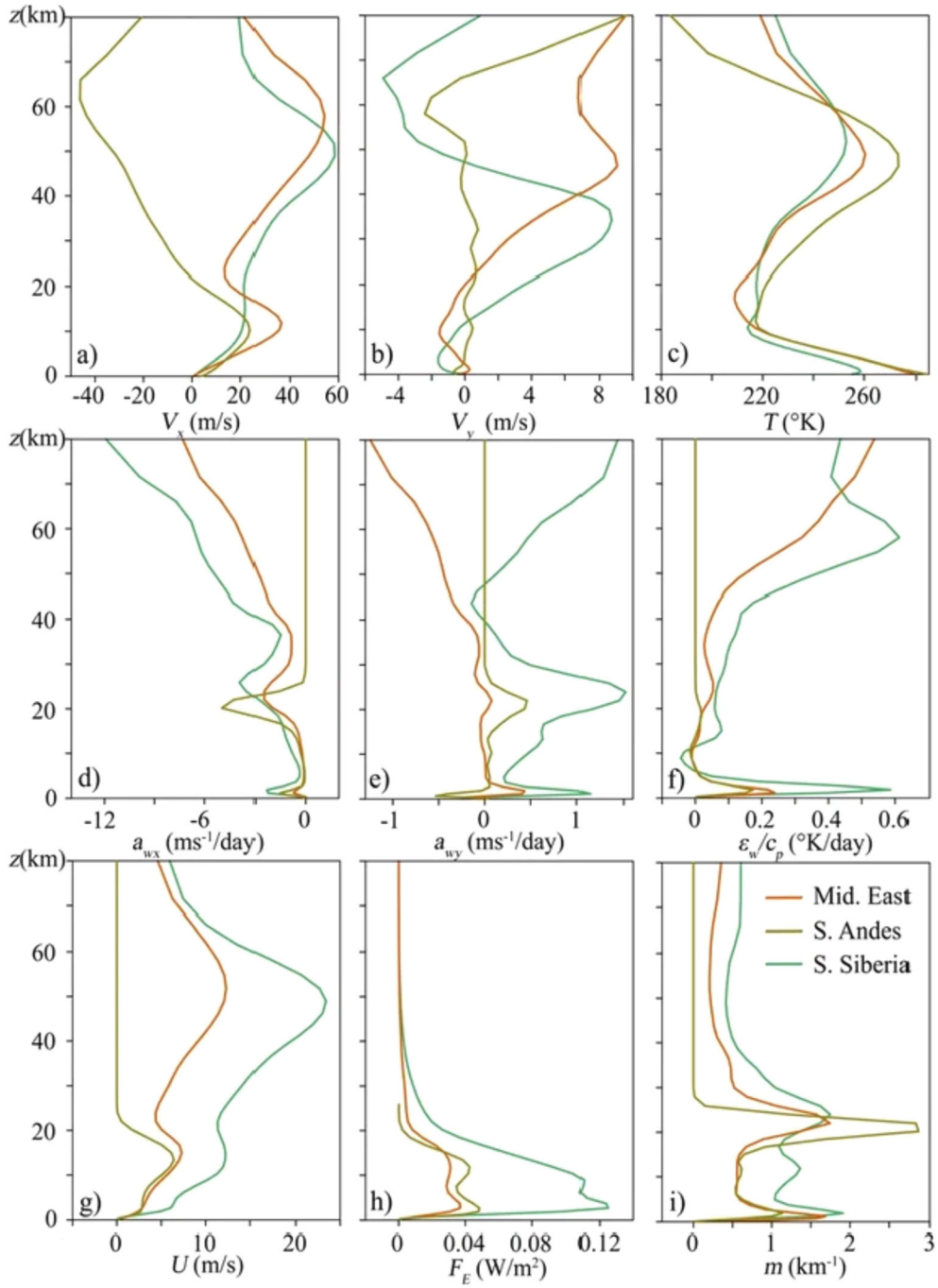

Figure 3
Vertical profiles of the background fields and OGW parameters at three locations shown by rectangles in Figs. 2, 3: background zonal (**a**) and meridional (**b**) wind components; background temperature (**c**); zonal (**d**) and meridional (e) OGW drag components; OGW heat influx (**f**); OGW velocity amplitude (**g**); vertical total energy flux (**h**); OGW vertical wavenumber (**i**)

three profiles are significantly different. The background temperature profiles in Fig. 3c are also different due to the difference in the geographical location of the regions under consideration. In the

troposphere, the temperature in the Southern Siberia is lower than that in the Middle East (located closer to the equator) and in the Southern Andes, where it is summer in January. In the stratosphere and mesosphere in Fig. 3c, the background temperature is higher in the Southern Hemisphere compared to that in the Northern Hemisphere.

Figure 3d presents the parameterized zonal component of OGW drag. It is negative in the regions of eastward background wind with its magnitude maximized at altitudes of 20–30 km in both hemispheres. In the Southern Hemisphere in Fig. 3d, the zonal wave drag is sharply decreased at altitudes above 20 km due to OGW filtering by summer easterlies (see above), while in the Northern Hemisphere, it is increasing in altitude after local minima at altitudes 30–40 km. This is connected with an increase in the background wind velocity inside the stratospheric jet stream in Fig. 3a. Similar vertical structure for altitudes up to 35 km was obtained by Van Niekerk et al. (2020) for the Middle East area. The meridional component of OGW drag in Fig. 3e is significantly different in different locations, which corresponds to the differences in the vertical profiles of the background meridional wind in Fig. 3b. In general, the magnitude of the meridional OGW drag in Fig. 3e is smaller than that for the zonal one in Fig. 3d.

The values of wave heat influxes in Fig. 3f are mostly positive in the Northern Hemisphere, which corresponds to estimates by Akmaev (2007), Hickey et al. (2011), Medvedev and Yiğit (2019), Gavrilov et al. (2020) showing the net heating of the atmosphere by gravity waves at altitudes below 150 km. In the upper troposphere over Southern Siberia, the parameter δ in Eq. (4) becomes negative and $\varepsilon_w < 0$ in Fig. 3f. OGW amplitudes in Fig. 3g reach maxima at altitudes of 50–60 km, above which OGW are significantly affected by increased viscosity and heat conduction, therefore waves are gradually dissipated.

The total wave energy flux, F_E, in Fig. 3h decreases quasi-exponentially with height above 25–30 km in all cases. This is due to increasing OGW viscous dissipation and changes in vertical wavenumber m according to Eq. (1). In addition, critical layers in the vicinity of heights, where $\bar{v}_\xi \to 0$, and OGW breaking in the regions of wave convective instability may prevent OGW propagation to high altitudes (see Sect. 2.1). Profiles of the vertical wavenumber obtained with Eq. (1) are shown in Fig. 3i. Mentioned factors of OGW dissipation are most pronounced in the summer Southern Hemisphere compared to the winter Northern Hemisphere, where more favorable conditions for the propagation of stationary OGWs exist (e.g., Pertsev, 1989).

The total wave energy flux in Fig. 3h is strongest over the Southern Siberia, because the mountains in this area are higher and the horizontal momentum flux and OGW amplitude in Eq. (8) at low boundary are larger (see Fig. 3g). The calculated horizontal OGW scales (from tens to hundreds km) are consistent with observational data, for example, with the data of Atmospheric Infrared Sounder (AIRS) over Europe (Heale et al., 2020) and with the data of the Gulfstream V project over New Zealand (Fritts et al., 2018, 2019), also with the data from the airglow imaging system of Boston University over Andes mountains (Smith et al., 2009).

Figure 3 shows that Eqs. (1–5) provide the nonzero wave drag and heat influx even for stationary OGWs, which are subject to dissipation according to background profiles of molecular and turbulent viscosity and heat conduction and changes in the vertical wavenumber m described by Eq. (1). Figure 3 shows also that OGW drag and heat influx given by the modified OGW parameterization have magnitudes, which are strong enough for modifications of the general circulation in the middle atmosphere. The influence of the modifications in the OGW parameterization on the mean fields of zonal wind and temperature simulated with the SOCOL3 chemistry-climate model are considered below.

4. *Influence of MSOP on the Background Fields in the SOCOL3 Model*

To analyze the influence of OGW parameterization on the mean climatological fields, the OGW parameterization MSOP with modifications described in Sect. 2 was implemented into the SOCOL3 model. Instant distributions of the background atmospheric wind, temperature, density and pressure for solving Eq. (5) are taken from the SOCOL3 model at each time step. To take into account OGW dynamical and

thermal effects, the zonal and meridional components of OGW drag were included into the SOCOL3 equations of motion and the OGW heat influx in °K/day was included as ε_w/c_p into the energy prognostic equation. Test simulations of the general atmospheric circulation for 10 years (from 2009 to 2018) were performed using the previous SSOP and new MSOP parameterization schemes. Similar 10-year simulation was also performed with turned off parameterization of OGW effects.

Figures 4 and 5 show the latitude-height distributions of the zonal-mean zonal wind and temperature averaged for January over 10 years, respectively. Figures 4a and 5a present the January zonal-mean zonal wind and temperature obtained from the MERRA2 reanalysis of meteorological information (Gelaro et al., 2017) and averaged for the same years that were modeled with SOCOL3. Panels 4b and 5b show respective distributions simulated with the SOCOL3 model without inclusion of OGW effects. One can see that without OGW influence, the zonal wind velocity (Fig. 4b) in the stratosphere becomes unrealistically high (up to 70 m/s) and the temperature in subpolar stratosphere (Fig. 5b) is significantly underestimated (up to 10 K) by the model.

Simulated zonal-mean zonal wind and temperature are shown in Figs. 4c and 5c for the previous SSOP and in Figs. 4d and 5d for the new MSOP schemes used in the SOCOL3 model. The inclusion of any OGW parameterization scheme into the model leads to a deceleration of the atmospheric circulation in the northern stratosphere, so that the magnitudes of zonal wind velocity in Fig. 4c and d become closer to those in the MERRA2 data shown in Fig. 5a. Simulated temperatures in Figs. 5c and 5d are also closer to the reanalysis data in Fig. 5a.

Figure 6a and d show differences of the 10-year average January zonal-mean zonal wind and temperature simulated with the SOCOL3 model without OGW effects and respective values for the MERRA2 meteorological reanalysis data. The shaded regions in Fig. 6 correspond to 90% statistical confidence of respective differences estimated with the Welch's t-test (Statistical Odds & Ends, 2020). This test is a modification of the Student's two-sample t-test assuming that the two analyzed populations may have different variances. In Fig. 6 the Welch's t-test is applied to monthly-mean differences obtained for January during 10-year simulations with the SOCOL3 model involving different OGW parameterizations. The magnitudes of differences in zonal wind in Fig. 6a and temperature in Fig. 6d exceed 20 m/s and 10 K, respectively, in the northern stratosphere, which are statistically significant with respect of the interannual model variability.

The differences of simulated and reanalysis mean zonal wind obtained for both SSOP and MSOP in Fig. 6b and c have smaller magnitudes in the Northern Hemisphere compared to Fig. 6a without OGW effects. Usage of the previous SSOP scheme gives the negative differences up to -6 m/s at high northern latitudes and positive differences up to 10 m/s at latitudes 20–40° N near pressure level of 1 hPa in Fig. 6b. For MSOP scheme, involving modifications described in Sect. 2, respective differences in Fig. 6c do not exceed ± 4 m/s in the Northern Hemisphere.

The differences of the zonal wind in Fig. 6b and c are closer for both SSOP and MSOP schemes in the Southern Hemisphere, where summer westward mean winds (see Fig. 4a) prevent upward propagation of stationary OGWs and, therefore, the wave drag tends to zero at altitudes above 20–25 km in summer (see Fig. 3d, e).

Figure 6e, f reveal that for both SSOP and MSOP schemes the differences of simulated and observed temperatures do not exceed ± 4 K below the pressure level of 0.7 hPa, which is smaller than the respective differences of ± (8–10) K at high northern latitudes in Fig. 6d for simulations with the SOCOL3 model without OGW effects. Above the pressure level of 0.7 hPa in Fig. 5b–d, the temperature distributions are very similar for both OGW parameterizations, showing that wave heating/cooling effects are relatively small there. The main temperature changes in Fig. 5b–d are seen at high northern latitudes at pressure levels 0.5–2 hPa, where the differences of simulated and observed temperature in Fig. 6e, f may reach ± 8 K for both SSOP and MSOP parameterizations.

The MSOP scheme includes diabatic heat influxes due to the dissipation of OGWs described by Eq. (3), (4). At the same time, Fig. 1 shows that mountain

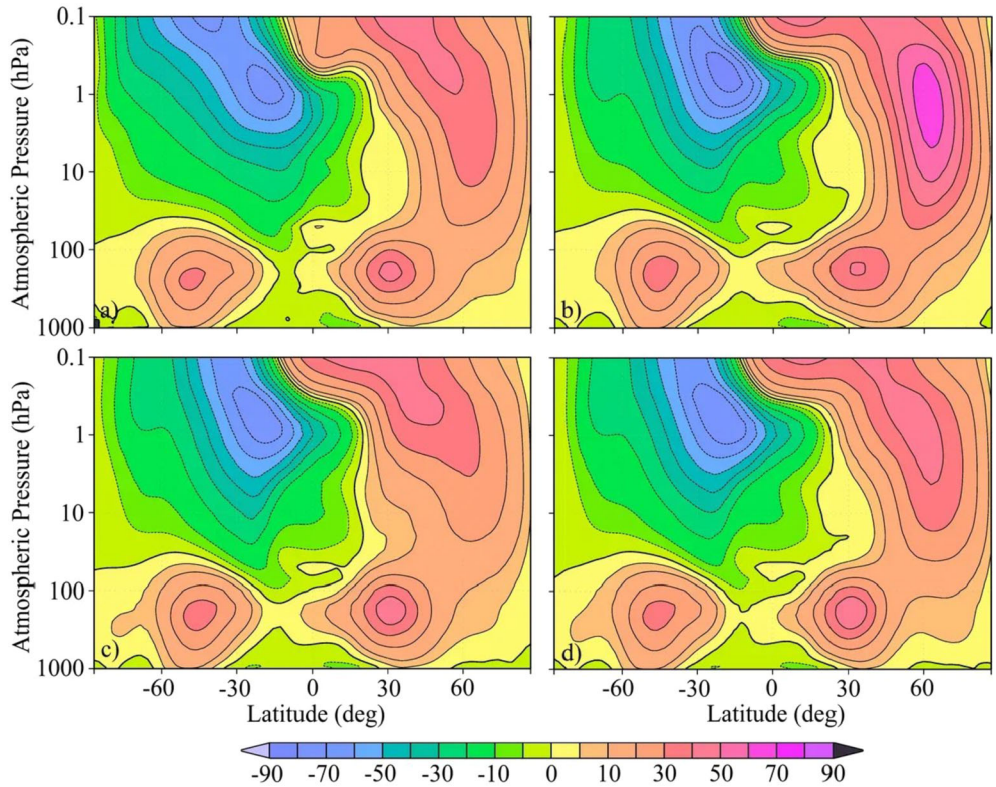

Figure 4
Latitude-altitude distributions of the zonal-mean zonal wind in m/s for January averaged over 10 years according to MERRA-2 data (**a**) and simulated using SOCOL3 model without OGW parameterization (**b**), with the previous SSOP (**c**) and new MSOP (**d**) schemes of OGW dynamical and thermal effects

OGW sources, amplitudes and, consequently, wave heat influxes do not maximize at high latitudes. One should keep in mind that because of the presence of Coriolis force in the SOCOL3 equation of motion, the zonal OGW drag shown in Fig. 2 and Fig. 3d may produce changes in the meridional atmospheric circulation and vertical velocity, which can influence diabatic heating/cooling in the high-latitude middle atmosphere. Therefore, modified meridional circulation may change the mean temperature distributions shown in Fig. 5c, d.

For simulating vertical profiles of wave characteristics, the SSOP scheme in the SOCOL3 model (see Sect. 2.3) uses ideas of saturated IGWs by Lindzen (1981) assuming that above the orographic source the OGW wave momentum flux is constant and wave drag is zero, except for critical and breaking levels, above which the wave stress is set to zero or remains constant and equal to the stress at the breaking level (see Sect. 2.3). Examples of vertical profiles of the OGW stress (proportional to F_m) obtained with SSOP one can find in Fig. 6 of the paper by Lott and Miller (1997).

The main difference of the new MSOP scheme is calculating more detailed vertical profiles of OGW characteristics and wave drag using Eqs. (1), (4), (5) at each node of horizontal grid of the SOCOL3 model. Unfortunately, direct comparisons of profiles of wave characteristics given by the SSOP and MSOP schemes are not possible, because the code of the SOCOL3 model does not allow output of necessary OGW parameters from the SSOP scheme. Using Eq. (5) in the MSOP scheme gives additional parameters (e.g., the turbulent viscosity and turbulent Prandtl number), which allow better adjustment of

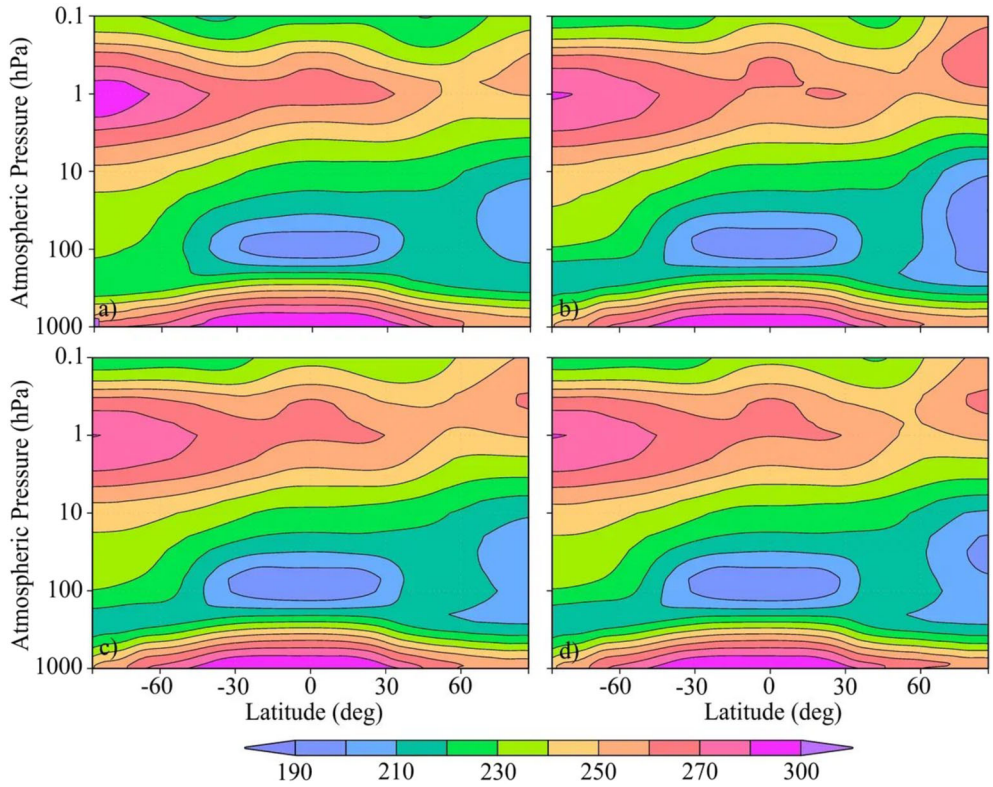

Figure 5
Same as Fig. 4, but for the zonal-mean temperature in °K

simulated atmospheric characteristics to the observed ones.

Described in this section results show that OGW dynamical and thermal effects and modifications of their parameterizations in the general circulation and climate models may influence simulated mean atmospheric characteristics. Further studies of OGWs, their parameterizations and wave-induced meridional circulation are required for decreasing discrepancies between simulated and observed zonal wind, temperature and composition in the region of the mesosphere and lower thermosphere.

5. *Conclusions*

In this study, modifications in the subgrid orographic wave parameterization is implemented into the SOCOL3 chemistry-climate model. The modified OGW parameterization, MSOP, is based on the Lott and Miller (1997) scheme, similarly to the SSOP scheme currently used in the SOCOL3 model and described by Roeckner et al. (2003). The MSOP scheme uses formulae for simulating vertical profiles of the amplitude of wave velocity variations, wave drag and heat influxes based on the polarization relations for mesoscale stationary OGWs in the rotating atmosphere obtained by Gavrilov and Koval (2013). Using the obtained with SOCOL3 realistic profiles of the background wind and temperature, characteristics of OGWs propagating in the atmosphere from the Earth's surface to the heights of about 80 km were simulated for different locations in the Northern and Southern Hemispheres. Peculiarities of OGW propagation from their sources in different regions and their impacts on the atmospheric circulation and thermal regime at heights up to the mesosphere are considered.

It is shown that OGW dynamical and thermal effects significantly contribute to the formation of the

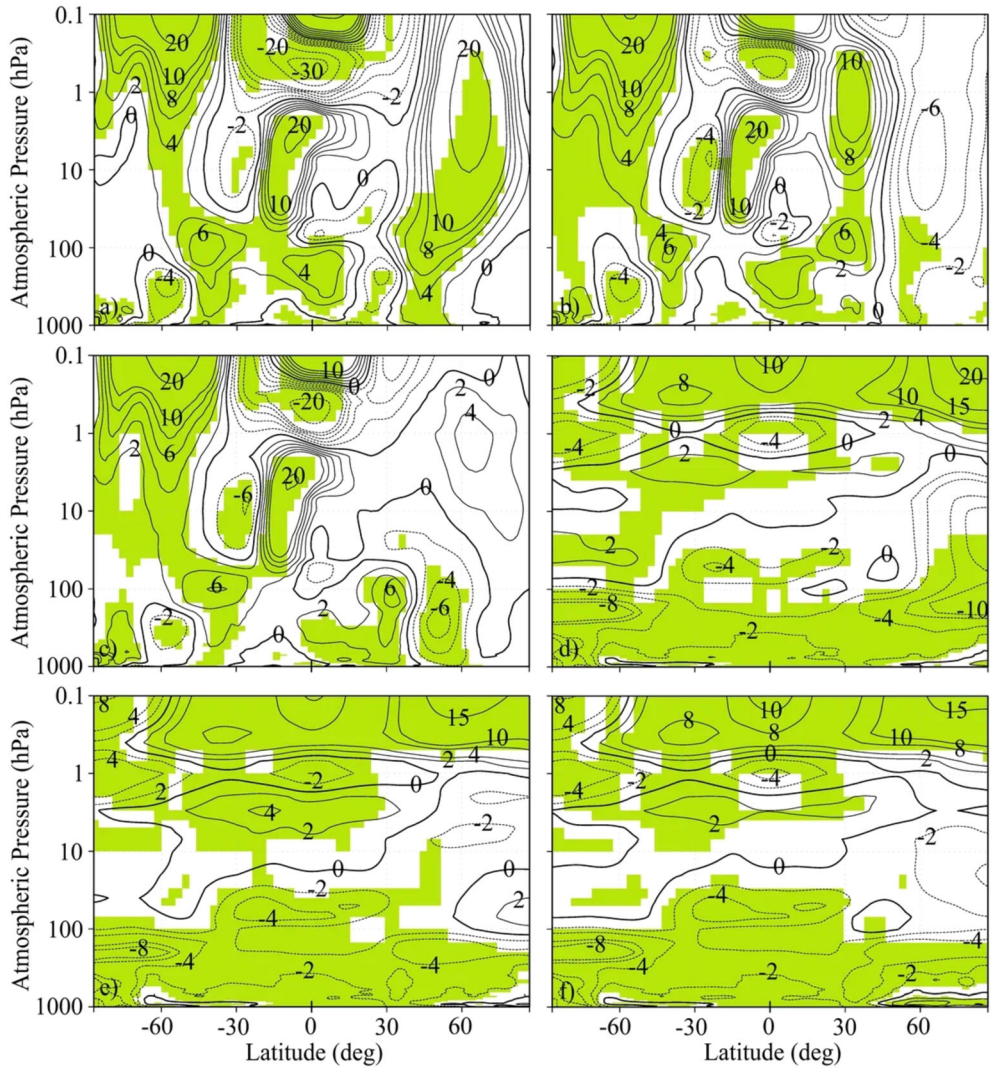

Figure 6

Differences of the zonal-mean zonal wind in m/s (**a–c**) and temperature in °K (**d–e**) simulated using the SOCOL3 model with no OGWs (**a, d**), with the previous SSOP (**b, e**), with the MSOP (**c, f**) and the respective values from the MERRA2 meteorological reanalysis data for January averaged for 10 years. Shaded areas correspond to differences with statistical significance higher than 90% according to the Welch's t-test criteria

general atmospheric circulation, reducing the velocity of jet stream in the winter middle atmosphere. When comparing with the MERRA-2 data, for the MSOP scheme the differences of simulated and reanalysis zonal-mean zonal wind does not exceed ± 4 m/s in the Northern Hemisphere in January compared to the respective differences up to ± (6–10) m/s for the previous SSOP scheme. The differences of simulated and reanalysis temperatures do not exceed ± 4 K below the pressure level of 0.7 hPa. The main changes in temperature fields for different OGW parameterizations occur at high northern latitudes at pressure levels of 0.5–2 hPa, where temperature differences of simulated and observed temperature may reach ± 8 K for both SSOP and MSOP schemes. Further studies of OGW effects and wave-induced meridional circulation are required for more accurate simulations of the general circulation and

climatological characteristics in the mesosphere and lower thermosphere.

Acknowledgements

In this study we used the data obtained in the SPbU resource center "Geomodel". All plots in this study were made using Grid Analysis and Display System (GrADS) which is a free software developed according to the NASA Advanced Information Systems Research Program.

Authors Contributions A.V.K.: development and testing of the parameterization; N.M.G.: conceptualization and consulting; V.A.Z.: implementation of the OGW parameterization into the model SOCOL and performing numerical simulations; E.V.R.: providing the SOCOL source code and consulting; A.G.G.: statistical analysis of the simulated data. All authors have read and agreed to the published version of the manuscript.

Funding

This study was supported by Saint-Petersburg State University (research grant 116234986) for implementing the MSOP parametrization into the SOCOL3 model and performing numerical simulations; also, by the Russian Science Foundation (grant #24-17-00230) for developing and testing the parametrization.

Data Availability

No datasets were generated or analysed during the current study.

Declarations

Conflict of interest The authors declare no competing interests.

References

Akmaev, R. A. (2007). On the energetics of the mean-flow interactions with thermally dissipating gravity waves. *Journal of Geophysical Research., 112*, 11125.

Alexander, M. J., & Teitelbaum, H. (2007). Observation of a large amplitude mountain wave event over the Antarctic Pennisula. *Journal of Geophysical Research, 112*, D21103. https://doi.org/10.1029/2006JD008368

Alexander, M. J., Geller, M., McLandress, C., Polavarapu, S., Preusse, P., Sassi, F., et al. (2010). Recent developments in gravity-wave effects in climate models and the global distribution of gravity-wave momentum flux from observations and models. *Quarterly Journal of the Royal Meteorological Society, 136*, 1103–1124. https://doi.org/10.1002/qj.637

Andrews, D. G., Leovy, C. B., & Holton, J. R. (1987). *Middle Atmosphere Dynamics* (p. 489). Spain: Academic Press.

Baines, P. G., & Palmer, T. N. (1990). Rationale for a new physically-based parametrization of subgridscale orographic effects. *Technical Memorandum*. https://doi.org/10.21957/h4h36b3u

Beer, T. (1974). *Atmospheric Waves* (p. 300). John Wiley Press.

Butchart, N. (2014). The Brewer-Dobson circulation. *Reviews of Geophysics, 52*, 157–184. https://doi.org/10.1002/2013RG000448

Butchart, N., Charlton-Perez, A. J., Cionni, I., Hardiman, S. C., Haynes, P. H., & Krüger, K. (2011). Multimodel climate and variability of the stratosphere. *Journal of Geophysical Research, 116*, D05102. https://doi.org/10.1029/2010JD014995

Choi, H. J., & Hong, S. Y. (2015). An updated subgrid orographic parameterization for global atmospheric forecast models. *Journal of Geophysical Research, 120*, 12445–12457. https://doi.org/10.1002/2015JD024230

Eckermann, S. D., & Preusse, P. (1999). Global measurements of stratospheric mountain waves from space. *Science, 286*(5444), 1534–1537. https://doi.org/10.1126/science.286.5444.1534

Egorova, T. A., Rozanov, E. V., Zubov, V. A., & Karol, I. L. (2003). Model for investigating ozone trends (MEZON). *Izvestiya Atmospheric and Oceanic Physics, 39*(3), 277–292.

ETOPO2. (2015). Gridded global 2-minute relief data. *National Geophysical Data Center, National Oceanic and Atmospheric Administration, U.S. Dept. of Commerce*. https://www.ngdc.noaa.gov/mgg/global/relief/ETOPO2/ETOPO2v2-2006 (last excess on January 20, 2024).

Fritts, D. C., Vosper, S. B., Williams, B. P., Bossert, K., Plane, J. M. C., Taylor, M. J., et al. (2018). Large-amplitude Mountain waves in the mesosphere accompanying weak cross-mountain flow during DEEPWAVE Research Flight RF22. *Journal of Geophysical Research: Atmospheres, 123*(9992–10), 022. https://doi.org/10.1029/2017JD028250

Fritts, D. C., Wang, L., Taylor, M. J., Pautet, P.-D., Criddle, N. R., Kaifler, B., et al. (2019). Large-amplitude mountain waves in the

mesosphere observed on 21 June 2014 during DEEPWAVE: 2. Nonlinear dynamics, wave breaking, and instabilities. *Journal of Geophysical Research, 124*, 10006–10032. https://doi.org/10.1029/2019JD030899

Gavrilov, N. M. (1990). Parameterization of accelerations and heat flux divergences produced by internal gravity waves in the middle atmosphere. *Journal of Atmospheric and Terrestrial Physics, 52*(9), 707–713. https://doi.org/10.1016/0021-9169(90)90003-6

Gavrilov, N. M., & Koval, A. V. (2013). Parameterization of mesoscale stationary orographic wave forcing for use in numerical models of atmospheric dynamics. *Izvestiya, Atmospheric and Oceanic Physics, 49*(3), 244–251. https://doi.org/10.1134/S0001433813030067

Gavrilov, N. M., & Popov, A. A. (2022). Modeling seasonal variations in the intensity of internal gravity waves in the lower thermosphere. *Izvestiya, Atmospheric and Oceanic Physics, 58*(1), 68–79. https://doi.org/10.1134/S0001433822010030

Gavrilov, N. M., Koval, A. V., Pogoreltsev, A. I., & Savenkova, E. N. (2015). Simulating influences of QBO phases and orographic gravity wave forcing on planetary waves in the middle atmosphere. *Earth, Planets and Space, 67*, 86. https://doi.org/10.1186/s40623-015-0259-2

Gavrilov, N. M., Kshevetskii, S. P., & Koval, A. V. (2020). Thermal effects of nonlinear acoustic-gravity waves propagating at thermospheric temperatures matching high and low solar activity. *Journal of Atmospheric and Solar-Terrestrial Physics, 208*, 105381. https://doi.org/10.1016/j.jastp.2020.105381

Gelaro, R., McCarty, W., Suárez, M. J., Todling, R., Molod, A., Takacs, L., et al. (2017). The modern-era retrospective analysis for research and applications, version 2 (MERRA-2). *Journal of Climate, 30*(14), 5419–5454. https://doi.org/10.1175/JCLI-D-16-0758.1

Gossard, E. E., & Hooke, W. H. (1975). *Waves in the atmosphere* (p. 456p). Elsevier Sci. Publ. Co.

Gregory, D., Shutts, G. J., & Mitchell, J. R. (1998). A new gravity wave-drag scheme incorporating anisotropic orography and low-level wave breaking: Impact upon the climate of the UK Meteorological Office Unified Model. *Quarterly Journal of the Royal Meteorological Society, 124*, 463–493. https://doi.org/10.1002/qj.49712454606

Heale, C. J., Bossert, K., Vadas, S. L., Hoffmann, L., Dörnbrack, A., Stober, G., et al. (2020). Secondary gravity waves generated by breaking mountain waves over Europe. *Journal of Geophysical Research, 125*, e2019JD031662. https://doi.org/10.1029/2019JD031662

Hegglin, M.I., Lamarque, J.F., & Eyring, V. (2015). The IGAC/SPARC chemistry-climate model initiative phase-1 (CCMI-1) model data output. *NCAS British Atmospheric Data Centre*, http://catalogue.ceda.ac.uk/uuid/9cc6b94df0f4469d8066d69b5df879d5. Accessed 10 Oct 2024

Hickey, M. P., Walterscheid, R. L., & Schubert, G. (2011). Gravity wave heating and cooling of the thermosphere: Sensible heat flux and viscous flux of kinetic energy. *Journal of Geophysical Research, 116*, A12326. https://doi.org/10.1029/2011JA016792

Hoffmann, L., Xue, X., & Alexander, M. J. (2013). A global view of stratospheric gravity wave hotspots located with Atmospheric Infrared Sounder observations. *Journal of Geophysical Research: Atmospheres, 118*, 416–434. https://doi.org/10.1029/2012JD018658

Jiang, J. H., Wu, D. L., & Eckermann, S. D. (2002). Upper Atmosphere Research Satellite (UARS) observation of mountain waves over the Andes. *Journal of Geophysical Research, 107*(D20), 8273. https://doi.org/10.1029/2002JD002091

Kaifler, B., Kaifler, N., Ehard, B., Dornbrack, A., Rapp, M., & Fritts, D. C. (2015). Influences of source conditions on mountain wave penetration into the stratosphere and mesosphere. *Geophysical Research Letters, 42*, 9488–9494. https://doi.org/10.1002/2015GL066465

Kikoin, I. K. (1976). *Tables of Physical Quantities* (pp. 272–279). Moscow: Atomizdat Press.

Kim, Y.-J., & Arakawa, A. (1995). Improvement of orographic gravity wave parameterization using a mesoscale gravity wave model. *Journal of the Atmospheric Science, 52*(11), 1875–1902.

Kim, Y. J., & Doyle, J. (2005). Extension of an orographic-drag parameterization scheme to incorporate orographic anisotropy and flow blocking. *Quarterly Journal of the Royal Meteorological Society, 131*, 1893–1921. https://doi.org/10.1256/qj.04.160

Kim, Y. J., Eckermann, S. D., & Chun, H. Y. (2003). An overview of the past, present and future of gravity-wave drag parametrization for numerical climate and weather prediction models. *Atmosphere- Ocean, 41*, 65–98. https://doi.org/10.3137/ao.410105

Kuchar, A., Sacha, P., Eichinger, R., Jacobi, Ch., Pisoft, P., & Rieder, H. E. (2020). On the intermittency of orographic gravity wave hotspots and its importance for middle atmosphere dynamics. *Weather and Climate Dynamics, 1*, 481–495. https://doi.org/10.5194/wcd-1-481-2020

Limpasuvan, V., Richter, J. H., Orsolini, Y. J., Stordal, F., & Kvissel, O.-K. (2012). The roles of planetary and gravity waves during a major stratospheric sudden warming as characterized in WACCM. *Journal of Atmospheric and Solar-Terrestrial Physics, 78–79*, 84–98. https://doi.org/10.1016/j.jastp.2011.03.004

Lindzen, R. S. (1981). Turbulence and stress due to gravity wave and tidal breakdown. *Journal of Geophysical Research, 86*, 9707–9714.

Lott, F., & Miller, M. J. (1997). A new subgrid-scale orographic drag parametrization: Its formulation and testing. *Quarterly Journal of the Royal Meteorological Society, 123*, 101–127.

Medvedev, A. S., & Klaassen, P. (2003). Thermal effects of saturating gravity waves in the atmosphere. *Journal of Geophysical Research, 108*(D2), 4040. https://doi.org/10.1029/2002JD002504

Medvedev, A. S., & Yiğit, E. (2019). Gravity waves in planetary atmospheres: Their effects and parameterization in global circulation models. *Atmosphere, 10*, 531. https://doi.org/10.3390/atmos10090531

Pertsev, N. N. (1989). Azimuth anisotropy of mountain lee waves in the upper atmosphere. *Izvestiya, Atmospheric and Oceanic Physics, 25*(6), 585–591.

Pertsev, N. N. (1997). Seasonal and height variations of orographically induced mesoscale fluctuations in the middle atmosphere. *Izvestiya, Atmospheric and Oceanic Physics, 33*(6), 722–728.

Preusse, P., Dornbrack, A., Eckermann, S. D., Riese, M., Schaeler, B., Bacmeister, J. T., et al. (2002). Space-based measurements of stratospheric mountain waves by CRISTA: 1. Sensitivity, analysis method, and a case study. *Journal of Geophysical Research, 107*(D23), 8178. https://doi.org/10.1029/2001JD000699

Reichert, B., Kaifler, N., Kaifler, M., et al. (2019). Retrieval of intrinsic mesospheric gravity wave parameters using lidar and

airglow temperature and meteor radar wind data. *Atmospheric Measurement Techniques, 12*(11), 5997–6015.

Roeckner, E., Bauml, G., Bonaventura, L., Brokopf, R., Esch, M., Giorgetta, M., et al. (2003). The atmospheric general circulation model ECHAM5, Part I, Model description. *Report No. 349, Max-Plank-Institute für Meteorologie, Hamburg*, 45–48. from https://pure.mpg.de/rest/items/item_995269_4/component/file_995268/content. Accessed on 01 June 2024

Schraner, M., Rozanov, E., Schnadt Poberaj, C., Kenzelmann, P., Fischer, A. M., Zubov, V., et al. (2008). Technical note: Chemistry-climate model SOCOL: version 2.0 with improved transport and chemistry/microphysics schemes. *Atmospheric Chemistry and Physics, 8*, 5957–5974. https://doi.org/10.5194/acp-8-5957-2008

Scinocca, J. F., & McFarlane, N. A. (2000). The parametrization of drag induced by stratified flow over anisotrophic orography. *Quarterly Journal of the Royal Meteorological Society, 126*(568), 2353–2393.

Scorer, R. S. (1949). Theory of waves in the lee of mountains. *Quarterly Journal of the Royal Meteorological Society, 75*, 41–56.

Semenov, A. I., Shagaev, M. V., & Shefov, N. N. (1981). On the effect of orographic waves on the upper atmosphere. *Izvestiya, Atmospheric and Oceanic Physics, 17*(9), 982–984.

Shefov, N. N., & Pertsev, N. N. (1984). Orographic disturbances of upper atmosphere emissions. *Handbook for MAP SCOSTEP, 10*, 171–175.

Shefov, N. N., Semenov, A. I., & Pertsev, N. N. (1999). Spatial distribution of igw energy inflow into the mesopause over the lee of a mountain ridge. *Geomagnetism and Aeronomy, 39*(5), 620–627.

Smith, S., Baumgardner, J., & Mendillo, M. (2009). Evidence of mesospheric gravity-waves generated by orographic forcing in the troposphere. *Geophysical Research Letters, 36*, L08807. https://doi.org/10.1029/2008GL036936

SPARC. (2010). SPARC CCMVal Report on the Evaluation of Chemistry- Climate Models, edited by: Eyring, V., Shepherd, T., & Waugh, D., SPARC Report No. 5, WCRP-30/2010, WMO/TD – No. 40, from https://www.sparc-climate.org/publications/sparc-reports/sparc-report-no-5/. Accessed on 1 June 2024

Statistical Odds & Ends. (2020). Welch's t-test and the Welch-Satterthwaite equation. *WordPress.com.*, from https://statisticaloddsandends.wordpress.com/2020/07/03/welchs-t-test-and-the-welch-satterthwaite-equation/. Accessed on 15 Sept 2024

Stenke, A., Schraner, M., Rozanov, E., Egorova, T., Luo, B., & Peter, T. (2013). The SOCOL version 3.0 chemistry–climate model: Description, evaluation, and implications from an advanced transport algorithm. *Geoscientific Model Development, 6*, 1407–1427. https://doi.org/10.5194/gmd-6-1407-2013

Sukhodoev, V. A., & Yarov, V. N. (1998). Temperature variations of the mesopause in the leeward region of the Caucasus ridge. *Geomagnetism and Aeronomy, 38*(4), 545–548.

Van Niekerk, A., Sandu, I., & Vosper, S. B. (2018). The circulation response to resolved versus parametrized orographic drag over complex mountain terrains. *Journal of Advances in Modeling Earth Systems, 10*(10), 2527–2547.

Van Niekerk, A., Sandu, I., Zadra, A., Bazile, E., Kanehama, T., Köhler, M., et al. (2020). Constraining orographic drag effects (COORDE): A model comparison of resolved and parametrized orographic drag. *Journal of Advances in Modeling Earth Systems, 12*(11), e2020MS002160.

Webster, S., Brown, A. R., Cameron, D. R., & Jones, C. P. (2003). Improvements to the representation of orography in the Met Office Unified Model. *Quarterly Journal of the Royal Meteorological Society, 129*, 1989–2010. https://doi.org/10.1256/qj.02.133

Xu, X., Song, J., Wang, Y., & Xue, M. (2017). Quantifying the effect of horizontal propagation of three-dimensional mountain waves on the wave momentum flux using Gaussian beam approximation. *Journal of the Atmospheric Sciences, 74*, 1783–1798. https://doi.org/10.1175/JAS-D-16-0275.1

Yiğit, E., & Medvedev, A. S. (2009). Heating and cooling of the thermosphere by internal gravity waves. *Geophysical Research Letters, 36*, L14807. https://doi.org/10.1029/2009GL038507

(Received July 6, 2024, revised October 13, 2024, accepted November 25, 2024)